This article has been accepted for publication in a future issue of this journal, but has not been fully edited. Content may change prior to final publication. Citation information: DOI 10.1109/TIA.2018.2856579, IEEE Transactions on Industry Applications

Analysis of Consequent Pole Spoke Type Vernier Permanent Magnet Machine with Alternating Flux Barrier Design

Wenbo Liu, *Student Member, IEEE,* Thomas A. Lipo, *Life Fellow, IEEE*

***Abstract*—The mechanism of torque production in the vernier machine is difficult to understand since the stator teeth originating flux modulation effects, upon which the torque is produced, are usually minor factors which are ignored in normal synchronous machines. This paper begins with an analytical study of a spoke type Vernier PM Machine (SVPM), which has a generic number of stator slots per pole per phase, upon which the key sizing equations are developed. An equivalent winding factor is defined to model stator teeth originating flux modulation phenomena and resulting multi-harmonic field coupling effects. Performance predictions and design observations concerning SVPMs are then obtained. A new topology for an SVPM using ferrite magnets is proposed where a consequent pole design having an alternating leakage flux blocking ability is developed for the rotor. Overall, this improved SVPM design significantly boosts the back-EMF compared to conventional SVPM, and the torque production even surpasses that of a benchmark rare earth IPM machine although with a slightly lower power factor.**

Keywords—alternating flux barrier; alternating rotor leakage; consequent pole; flux blocking; ferrite magnet; high torque density low speed; spoke type; vernier machine

NOMENCLATURE

$\boldsymbol{\theta_s}$	Spatial angle of the stator MMF.
$\boldsymbol{\theta_r}$	Spatial angle of the rotor magnet MMF.
$\boldsymbol{\theta_{rm}}$	Mechanical rotor rotation angle.
$\boldsymbol{k_h}$	h^{th} harmonic winding factor.
$\boldsymbol{k_w^{equiv}}$	Equivalent winding factor.
$\boldsymbol{N_s}$	Total number of turns per phase.
$\boldsymbol{I_{pk}}$	Stator peak current.
$\boldsymbol{C_p}$	Number of parallel circuits.
$\boldsymbol{P_s}$, $\boldsymbol{P_r}$	Number of stator poles, and number of rotor poles.
$\boldsymbol{S_s}$	Number of stator slots.
$\boldsymbol{\gamma}$	Current phase shift angle.
$\boldsymbol{\gamma_0}$	Stator slot pitch angle.
$\boldsymbol{\hat{p}_0}$, $\boldsymbol{\hat{p}_h}$	*dc* and h^{th} harmonic component of relative permeance
$\boldsymbol{l_{stk}}$	Stack length.

I. INTRODUCTION

The vernier machine which was first introduced as a precision angle transducer in 1957 [1] utilizes a reluctance rotor topology with a high tooth count. The first application as a motor using a similar structure was reported in 1963 [2]. Although the large number of rotor teeth may appear to be the design requirement for operation of such a motor, these Vernier machines actually can be driven as a normal poly-phase synchronous machine, and operate on the principle of a Vernier gauge at the same time, given the fact that the stator and rotor pole number are different. In other words, the vernier machine effectively works as an electric gear, where the motor torque steps up as the rotor speed steps down from the usual synchronously rotating field. This feature makes it an ideal candidate for low speed, high torque direct drive systems.

As a relatively new type of electric machine, the torque density of the vernier machine has been improved about 11 times over the years, as the research on this type of machine has been extended to applying different excitation methods and structure topologies. Three major advancements have been achieved during this development era. The first advancement is to utilize the rotor field torque rather than the reluctance torque by replacing rotor reluctance teeth [1], [2] with surface mounted magnets [3]–[5]. A dual excitation/double stator structure [6] and double rotor structure [7] were then proposed to further boost torque density when extra airgap areas were provided for torque production. The third advancement has been the adoption of spoke type magnets in the double stator structure [8], which produces the highest torque density to date. The design uses an opposing magnet arrangement on the rotor such that the flux focusing effect is enabled. As a result, thick ferrite magnets are found to be also a suitable alternative for a flux source, which produces good torque density and possesses decent fault tolerant capability [9], [10]. Meanwhile, other attempts to improve torque capability have also been pursued. A hybrid type excitation method was proposed in [11] with the aim to combine the reluctance torque with field torque, where both windings and magnets are placed on the stator. Another attempt is the axial flux design with a multi-stator/rotor structure [12]. While the torque density of Vernier machines has been greatly improved, its complicated structure remains a hurdle for industry adoption.

During the six decades of development, various methods have been adopted to characterize the electromagnetic properties of the vernier machine, mainly through finite element analysis based parametric studies and sizing equation based analytical models, to investigate the impact of key machine parameters on performance. However, the parametric studies conducted with FEA were mostly target function-oriented and time-consuming, which also lacks generalization across the field of design parameters [9]. On the other hand, the analytical models thus

This article has been accepted for publication in a future issue of this journal, but has not been fully edited. Content may change prior to final publication. Citation information: DOI 10.1109/TIA.2018.2856579, IEEE Transactions on Industry Applications

reported are either constrained to specific electromagnetic quantities as in [3], [13], [14], or limited in its generalization of slot/pole combinations [5],[15],[13]. Furthermore, the developed analytical models generally lack physical insights into vernier machine design due to self-defined intermediate coefficients [13], [14], [16], [17]. Thus, a true physics-based model has not yet been established, nor does the characterization of a generic vernier machine which includes key design parameters.

The purpose of this paper is twofold. First, an analytical study of a generic spoke type vernier PM machine is presented, which has an arbitrary number of stator slots per pole per phase. Physics-based sizing equations are developed, where an equivalent winding factor is defined to model stator teeth originating flux modulation effects and multi-harmonic fields coupling effects. Two generic gear ratio designs are identified and compared. Performance predictions and design observations of vernier PM machines are obtained. Second, a novel spoke type vernier permanent magnet machine (SVPM), which uses ferrite magnets with an alternating rotor leakage flux blocking design is proposed and two gear ratio designs are compared. Key results are benchmarked against a conventional ferrite SVPM and an existing low-speed commercially available IPM using rare earth magnets.

II. Stator Teeth Originated Flux Modulation Effects

With an ideal smooth rotor, the flux density distribution in the air gap can be modeled having a constant value B_0, as shown in Fig. 1, which corresponds to that of a north pole of the rotor. However, in practice, a slotted stator is required to secure the stator windings. The slotted iron regions at the airgap will cause a flux density reduction in that portion, which can be described with an increased effective airgap length g_e. This approach, that was originally proposed by F. W. Carter [18], is mainly valid for characterization of the average flux density B_{avg} variations compared to B_0 in a machine with an ideal smooth airgap g. Assuming an open slot stator and smooth rotor machine, as shown with a partial model in Fig. 2(a), where the rotor north pole is aligned and opposing the stator slot, and by adopting Carter's coefficient k_c, as indicated by Fig. 2(b), one can obtain

$$g_e = k_c g\,,\ k_c = B_0 / B_{avg} \tag{1}$$

However, the actual flux density distribution along the airgap circumference is more concentrated under the stator teeth than the slots, as shown in Fig. 3(b) due to the much higher permeability of iron teeth, acting as that the rotor flux is modulated. To account for such stator teeth originated airgap flux density variations, a unitless quantity, i.e. a relative permeance $\hat{p}$ may be used, the definition for which is

$$\hat{p} = B(\theta_s) / B_0 = f(\theta_s) \tag{2}$$

In other words, instead of modeling the average flux density variation with the Carter's coefficient, the spatial distribution of flux density can be expressed as a function of the stator angle θ_s.

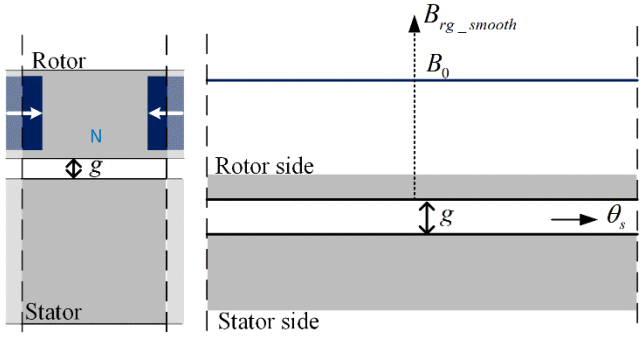

(a) Smooth airgap (b) Corresponding flux density distribution

Fig. 1. Modeling of a smooth airgap for one magnetic pole

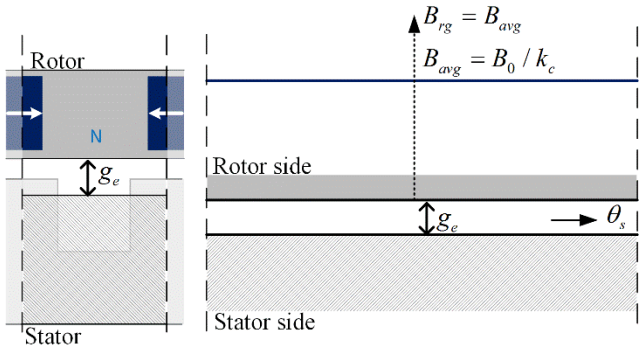

(a) Slotted airgap (b) Averaged flux density distribution

Fig. 2. Modeling of a slotted air gap for one magnetic pole using Carter's coefficient

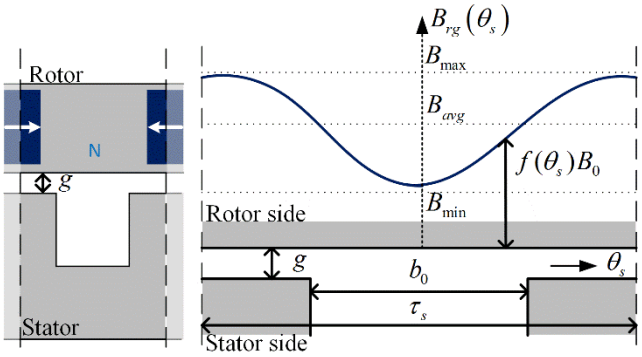

(a) Slotted airgap (b) Actual flux density distribution

Fig. 3. Modeling of a slotted airgap for one magnetic pole considering flux modulation effects

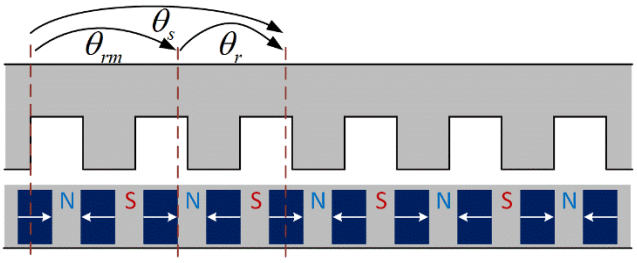

Fig. 4. Linearized model of a consequent pole PM machine

If one ignores the leakage and fringing effects, then for a specific consequent pole design as shown in Fig. 4, the relative

This article has been accepted for publication in a future issue of this journal, but has not been fully edited. Content may change prior to final publication. Citation information: DOI 10.1109/TIA.2018.2856579, IEEE Transactions on Industry Applications

permeance $\hat{p}$ can be explicitly written as the sum of harmonic components based on the stator slot number S_s [19]

$$\hat{p} = f(\theta_s) = \sum_{h=0}^{\infty} \hat{p}_h \cos(hS_s\theta_s) \tag{3}$$

where the magnitude of each component $\hat{p}_h$ is determined by the key slot geometry (i.e. τ_s, b_0, g) as identified in Fig. 3(b). Given that the magnet induced airgap flux density distribution B_{rg_smooth} in a slotless airgap is

$$B_{rg\_smooth} = \sum_{i=1}^{\infty} B_{mi} \sin\left(i\frac{P_r}{2}\theta_r\right) \tag{4}$$

the resultant airgap flux density B_{rg} due to the slot effects can be expressed as the product of (3) and (4) as

$$\begin{aligned} B_{rg} &= B_{rg\_smooth}\hat{p} \\ &= \sum_{i=1}^{\infty}\sum_{h=0}^{\infty} \hat{p}_h B_{mi} \sin\left(i\frac{P_r}{2}\theta_r\right)\cos(hS_s\theta_s) \end{aligned} \tag{5}$$

Setting $\theta_s - \theta_r = \theta_{rm}$, (5) becomes:

$$\begin{aligned} B_{rg} = \sum_{i=1}^{\infty}\sum_{h=0}^{\infty} \frac{B_{mi}\hat{p}_h}{2}\Bigg[&\sin\left(\left(i\frac{P_r}{2}+hS_s\right)\theta_s - i\frac{P_r}{2}\theta_{rm}\right) \\ &+\sin\left(\left(i\frac{P_r}{2}-hS_s\right)\theta_s - i\frac{P_r}{2}\theta_{rm}\right)\Bigg] \end{aligned} \tag{6}$$

Extra spatial harmonics of the air gap B field (with respect to θ_s) show up in (6) compared to (4), which can be considered as result of a stator teeth originated spatial modulation of the magnet induced airgap flux. These extra harmonic B fields generally exist in an machines having an open slot stator and round rotor structure, but they are normally ignored for the purpose of torque production. However, this effect will be important in a vernier machine as will be demonstrated in the following section.

Furthermore, the resultant air gap B field (6) can be simplified by excluding higher harmonics in (3) and (4), and only retaining the *dc* and fundamental (h = 0, 1) components in (3) with the fundamental component (i = 1) in (4), which has the largest magnitude. Then (6) becomes

$$\begin{aligned} B_{rg} = B_{m1}\Bigg[&\frac{1}{2}\hat{p}_1 \sin\left(\left(\frac{P_r}{2}-S_s\right)\theta_s - \frac{P_r}{2}\theta_{rm}\right) + \\ &\hat{p}_0 \sin\left(\frac{P_r}{2}(\theta_s-\theta_{rm})\right) + \frac{1}{2}\hat{p}_1 \sin\left(\left(\frac{P_r}{2}+S_s\right)\theta_s - \frac{P_r}{2}\theta_{rm}\right)\Bigg] \end{aligned} \tag{7}$$

where B_{m1} is determined by the magnet material and usage. The relative permeance can be explicitly expressed as functions of slot geometries namely $\hat{p}_0(b_0/\tau_s, b_0/g)$ and $\hat{p}_1(b_0/\tau_s, b_0/g)$. This procedure has been thoroughly studied and the details can be found in [19], [20]. Thus, the analytical form of the resultant airgap B field is readily defined. For certain simple slot shapes, the relative permeance can be calculated with given parameters as shown in Fig. 5. The results suggest that: $\hat{p}_0$ is 1 and $\hat{p}_1$ is 0 with smooth/slotless stator when b_0/τ_s or b_0/g is 0, corresponding to an absence of permeance variations. The difference between $\hat{p}_0$ and $\hat{p}_1$ begins to decrease as b_0/g and b_0/τ_s increases, corresponding to a progressively larger permeance variation in the airgap.

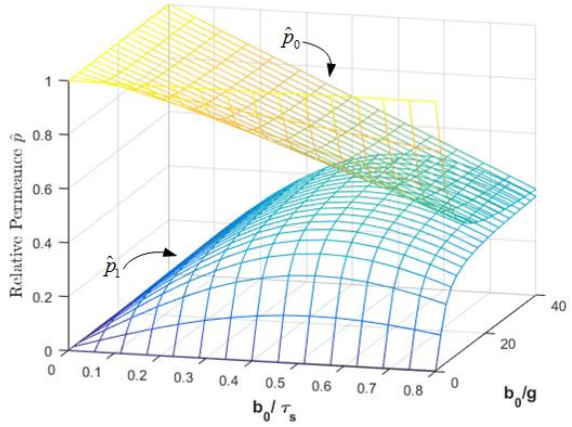

Fig. 5. Parametric study of the dc and fundamental components of relative permeance

III. Physics-Based Sizing Equations

To establish proper design principles for a generic spoke type vernier machine, an analysis utilizing physics based sizing equations has been adopted in this study, where a generic winding function is first developed, followed by flux linkage/back-EMF induction and torque production. An equivalent winding factor is defined to characterize the flux modulation effects.

A. Generic Form of Winding Function

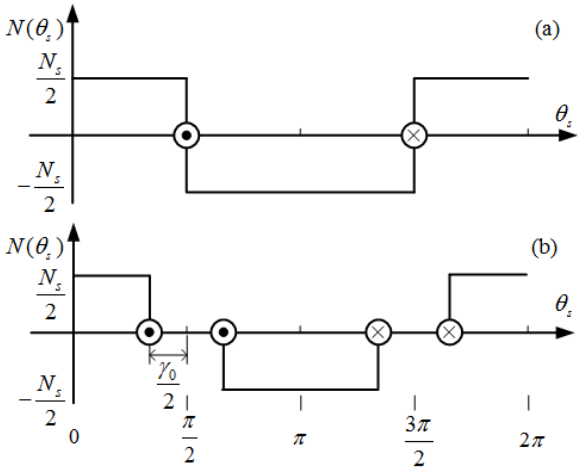

Fig. 6. Building blocks for a generic winding function

The winding function is developed as a generic model with an arbitrary number of slots per pole per phase (SPP) i.e. its q value, such that the effects of different slot/pole combinations can be included in the analysis. There are generally two building blocks to derive an analytical form of the generic winding function in a per phase fashion. One concerns the use of a full-pitch concentrated winding. It is constructed as an even function, where an ideal step change of the value of winding turns occurs at positions windings are placed, as shown in Fig.

This article has been accepted for publication in a future issue of this journal, but has not been fully edited. Content may change prior to final publication. Citation information: DOI 10.1109/TIA.2018.2856579, IEEE Transactions on Industry Applications

6(a), the expression of which can be represented by a Fourier Series as

$$N(\theta_s)=\frac{2N_s}{\pi}\sum_{h=1,3,5...}^{\infty}\frac{\sin(h\pi/2)}{h}\cos(h\theta_s) \quad (8)$$

The other building block is the distributed winding having pitch angle γ_0, where the step function is defined in the similar manner as shown in Fig. 6(b). It can be considered as an N_s turn winding which is split into two strands, each of which has half of the turns. The corresponding expression is:

$$N(\theta_s)=\frac{2N_s}{\pi}\sum_{h=1,3,5...}^{\infty}\frac{\sin((\pi-\gamma_0)h/2)}{h}\cos(h\theta_s) \quad (9)$$

where $\gamma_0=\pi/3q$.

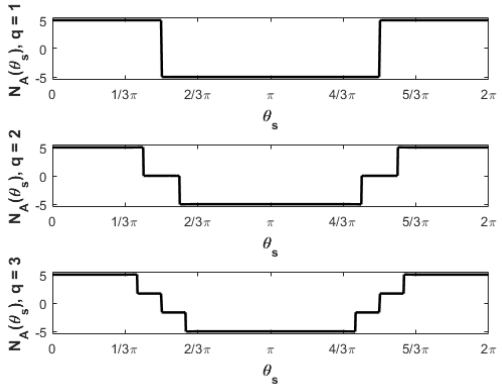

Fig. 7. Single layer winding function with a 60-degree phase belt

Assume that the stator only has one winding layer resulting in a 60-degree phase belt. A stepwise winding function with an arbitrary q number can then be represented as the sum of a series of building blocks as (8) and (9). The generic form for $N(\theta_s)$ with respect to P_s stator poles and q SPP value can be written as

$$N(\theta_s)=\frac{2}{\pi}N_s\sum_{h=1,3,5...}\frac{k_h}{h}\cos\left(h\frac{P_s}{2}\theta_s\right) \quad (10)$$

where the winding factor k_h is a function of q. If q = 1:

$$k_h=\sin\left(\frac{h\pi}{2}\right) \quad (11)$$

If q is even:

$$k_h=\frac{2\sin(hq\gamma_0/4)\sin(h(2\pi-q\gamma_0)/4)}{q\sin(h\gamma_0/2)} \quad (12)$$

If q is odd and larger than 1:

$$k_h=\frac{-\cos(h\pi/2)\cos(h\gamma_0/2)-\cos(h(\pi-q\gamma_0)/2)}{q\sin(h\gamma_0/2)} \quad (13)$$

The results from (10) to (13) suggest that, for q larger than unity, there is a slot pitch angle γ_0 introduced (assuming a full pitch winding configuration). The winding functions are verified and plotted on a 2-pole base in Fig. 7, for different q values and $N_s = 10$ per phase. The corresponding k_h for the first six harmonics are tabulated in Table. I.

TABLE I. WINDING FACTOR COEFFICIENT

k_h	q = 1	q = 2	q = 3	q = 4
1st	1.00	0.97	0.96	0.96
3rd	-1.00	-0.71	-0.67	-0.65
5th	1.00	0.26	0.22	0.21
7th	-1.00	0.26	0.18	0.16
9th	1.00	-0.71	-0.33	-0.27
11th	-1.00	0.97	0.18	0.13

The observations are:

- The higher order harmonics in k_h become reduced significantly as q increases.
- There are sign changes in different harmonic orders with certain choices of q.

Although a single layer winding is assumed, the modeling can be extended to other winding configuration using the same building blocks methodology.

B. *No-Load Flux Linkage and Back-EMF Induction in Two Gear Ratio Designs*

With the airgap flux density $B_{rg}(\theta_s,\theta_{rm})$ and winding function $N(\theta_s)$ both obtained, a generic form of flux linkage can then be found by integrating an incremental flux linkage $d\lambda$ over the stator circumference. Over one stator pole $d\lambda=\frac{1}{2}D_{is}l_{stk}\int_0^{2\pi/P_s}N(\theta_s)B_{rg}(\theta_s,\theta_{rm})\,d\theta_s$, assuming stator coils per phase are series connected. The total flux linkage is then written as

$$\begin{aligned}\lambda&=P_s\int_0^{2\pi/P_s}d\lambda=\frac{1}{2}D_{is}l_{stk}P_s\int_0^{2\pi/P_s}N(\theta_s)B_{rg}(\theta_s,\theta_{rm})d\theta_s\\&=\frac{D_{is}l_{stk}N_sB_{m1}P_s}{\pi}\int_0^{2\pi/P_s}\left(\sum_{h=1,3,5...}^{\infty}\frac{k_h}{h}\cos\left(h\frac{P_s}{2}\theta_s\right)\times p_{sum}d\theta_s\right)\end{aligned} \quad (14)$$

Given that

$$\begin{aligned}p_{sum}=&\frac{\hat{p}_1}{2}\sin\left(\left(\frac{P_r}{2}-S_s\right)\theta_s-\frac{P_r}{2}\theta_{rm}\right)+\hat{p}_0\sin\left(\frac{P_r}{2}(\theta_s-\theta_{rm})\right)\\&+\frac{\hat{p}_1}{2}\sin\left(\left(\frac{P_r}{2}+S_s\right)\theta_s-\frac{P_r}{2}\theta_{rm}\right)\end{aligned} \quad (15)$$

where the stator inner diameter D_{is} is used to approximate the airgap dimension for a inner-rotor machine configuration, and l_{stk} is stack length.

A physical interpretation of (14) is that multiple spatial harmonics of airgap B field can be coupled with the stator winding. To utilize as much flux linkage as possible, it is preferred to couple the lower order harmonics, since their magnitudes are inversely proportional to their harmonic order. This observation suggests that the fundamental component of winding function (10) and the lowest order of airgap B field (7) should share the same spatial frequency. Thus, the corresponding acceptable slot/pole combinations are:

This article has been accepted for publication in a future issue of this journal, but has not been fully edited. Content may change prior to final publication. Citation information: DOI 10.1109/TIA.2018.2856579, IEEE Transactions on Industry Applications

$$P_s/2 = \pm\left(P_r/2 - S_s\right) \tag{16}$$

where '$\pm$' designs are included since they both produce the same field spatial distribution.

In a balanced three-phase machine with $S_s = 3P_s q$, equation (16) can be simplified to an effective gear ratio between rotor pole number P_r and stator pole number P_s as:

$$\frac{P_r}{P_s} = 6q \pm 1 \tag{17}$$

corresponding to plus sign and minus sign design. The flux linkage can then be explicitly expressed as

$$\lambda = D_{is} l_{stk} N_s B_{m1} \frac{1}{2}\left(\frac{k_1}{1}\hat{p}_1 + \frac{2k_{6q\pm1}}{6q\pm1}\hat{p}_0 + \frac{k_{12q\pm1}}{12q\pm1}\hat{p}_1\right)\times \cos\left(\frac{P_r\theta_{rm}}{2} + \frac{\pi}{2}\right) \tag{18}$$

The result suggests that all three major airgap B fields couple with different winding harmonics, and contribute to the flux linkage induction both in plus sign design and minus sign design as shown in the parenthesis in (18). The corresponding harmonic orders are fundamental, $6q \pm 1\ th$ and $12q \pm 1\ th$, each of which are multiplied by a unitless relative permeance term to account for the flux modulation effects originated by the stator. Thus, the sum of the quantities in the parenthesis essentially characterize the effectiveness of flux linkage induction in the stator coil in the manner of a winding factor, which is effectively a product of a relative permeance vector and a harmonic winding factor vector. The overall product can be conveniently defined as an *equivalent winding factor*

$$k_w^{equiv} = \mathbf{p}\times\mathbf{k}^{\mathrm{T}} = \left[\frac{1}{2}\hat{p}_1 \quad \hat{p}_0 \quad \frac{1}{2}\hat{p}_1\right]\times\begin{bmatrix}\frac{k_1}{1}\\ \frac{k_{6q\pm1}}{6q\pm1}\\ \frac{k_{12q\pm1}}{12q\pm1}\end{bmatrix} = \frac{1}{2}\left(\frac{k_1}{1}\hat{p}_1 + \frac{2k_{6q\pm1}}{6q\pm1}\hat{p}_0 + \frac{k_{12q\pm1}}{12q\pm1}\hat{p}_1\right) \tag{19}$$

The back-EMF seen in the stator winding can then be calculated as the rate of change of no-load flux linkage over time as

$$e = \frac{d\lambda}{dt} = \frac{d\lambda}{d\theta_{rm}}\frac{d\theta_{rm}}{dt} = \omega_{rm}\frac{d\lambda}{d\theta_{rm}} = D_{is} l_{stk} N_s B_{m1}\frac{P_r}{2}\omega_{rm} k_w^{equiv}\cos\left(\frac{P_r\theta_{rm}}{2} + \pi\right) \tag{20}$$

With $\theta_{rm} = \omega_{rm} t$, (19) becomes

$$e = D_{is} l_{stk} N_s B_{m1}\frac{P_r}{2}\omega_{rm} k_w^{equiv}\cos\left(\frac{P_r}{2}\omega_{rm} t + \pi\right) \tag{21}$$

Thus, a parameter-based back-EMF equation has been established, where the term $D_{is} l_{stk}$ is the sizing coefficient which relates to machine dimensions, N_s is winding turns per phase value, B_{m1} is fundamental component of magnet induced airgap flux density, $P_r\omega_{rm}/2$ is the synchronous excitation frequency, and k_w^{equiv} is the equivalent winding factor that models multiple harmonic coupling effects, flux modulation effects and SPP value (gear ratio effects).

C. Torque Production

One means to model the torque production in electric machines considering flux modulation effects is, to start with energy storage in the rotating electromagnetic system as:

$$W = \frac{1}{2\mu_0}\int_V B^2 dV \tag{22}$$

The torque produced in the rotating magnetic field is then:

$$T = \frac{\partial W}{\partial\theta_{rm}} \approx \frac{D_{is} l_{stk}}{2}\int_0^{2\pi}\left(\frac{\partial}{\partial\theta_{rm}}B_{rg}\right)F_s d\theta_s \tag{23}$$

where B_{rg} is the airgap flux density in (7), and F_s is the stator MMF derived in [21] as:

$$F_s = \sum_{h=1,5,7,11\ldots}\left(\frac{6}{\pi}\right)\frac{k_h N_s I_{pk}}{hC_p P_s}\cos\left(h\frac{P_s}{2}\theta_s \pm \left(\omega_e t - \gamma\right)\right) \tag{24}$$

Since the peak surface current density K_s is expressed as

$$K_s = \frac{6N_s I_{pk}}{\pi D_{is}} \tag{25}$$

By substituting (7), (24), (25) into (23), the torque expression becomes

$$T = \frac{\pi D_{is}^2 l_{stk}}{4} K_s B_{m1}\frac{P_r}{P_s} k_w^{equiv}\cos\left(\frac{P_r}{2}\theta_{rm} \mp \omega_e t - \gamma\right) \tag{26}$$

The results indicate that average torque can be produced in both gear ratio designs, where the stator current must either rotate synchronously at the speed $\omega_e = P_r\theta_{rm}/(2t) = P_r\omega_{rm}/2$, which corresponds to the plus sign design having the gear ratio $P_r/P_s = 6q + 1$, or rotate in the reverse rotation direction of rotor, at the speed $\omega_e = P_r\omega_{rm}/2$, which corresponds to the minus sign design that produces the gear ratio $P_r/P_s = 6q - 1$.

Thus, a physical parameter-based torque equation has been derived where the term $\pi D_{is}^2 l_{stk}/4$ is the sizing coefficient which relates to rotor volume, K_s is the peak surface current density, B_{m1} is the fundamental component of magnet induced airgap flux density, P_r/P_s is the gear ratio that is a function of the SPP value with two design options, and k_w^{equiv} is the same equivalent winding factor as in (19).

D. Design Consideration of the Equivalent Winding Factor

It has been shown that both induced back-EMF and torque production are proportional to an equivalent winding factor, which is readily configured as the product of relative permeance vector and winding factor harmonic vector in (19). Based on the choice of gear ratios, this equivalent winding factor can be categorized into two forms as shown in Table. II, in which the multi-harmonic fields coupling effect is represented by the winding factor harmonic vector.

This article has been accepted for publication in a future issue of this journal, but has not been fully edited. Content may change prior to final publication. Citation information: DOI 10.1109/TIA.2018.2856579, IEEE Transactions on Industry Applications

TABLE II. EQUIVALENT WINDING FACTOR

		Plus sign design	Minus sign design
Gear ratio		$6q+1$	$6q-1$
k_w^{equiv}		$\mathbf{p}\times\mathbf{k}^{\mathrm{T}}=\frac{1}{2}\left(\frac{k_1}{1}\hat{p}_1+\frac{2k_{6q+1}}{6q+1}\hat{p}_0+\frac{k_{12q+1}}{12q+1}\hat{p}_1\right)$	$\mathbf{p}\times\mathbf{k}^{\mathrm{T}}=\frac{1}{2}\left(\frac{k_1}{1}\hat{p}_1+\frac{2k_{6q-1}}{6q-1}\hat{p}_0+\frac{k_{12q-1}}{12q-1}\hat{p}_1\right)$
Relative permeance vector		$\mathbf{p}=\left[\frac{1}{2}\hat{p}_1 \quad \hat{p}_0 \quad \frac{1}{2}\hat{p}_1\right]$	
Winding factor harmonic vector		$\mathbf{k}=\left[\frac{k_1}{1} \quad \frac{k_{6q+1}}{6q+1} \quad \frac{k_{12q+1}}{12q+1}\right]$	$\mathbf{k}=\left[\frac{k_1}{1} \quad \frac{k_{6q-1}}{6q-1} \quad \frac{k_{12q-1}}{12q-1}\right]$
Order of coupling harmonic components	Harmonic 1	fundamental	fundamental
	Harmonic 2	$6q+1$	$6q-1$
	Harmonic 3	$12q+1$	$12q-1$

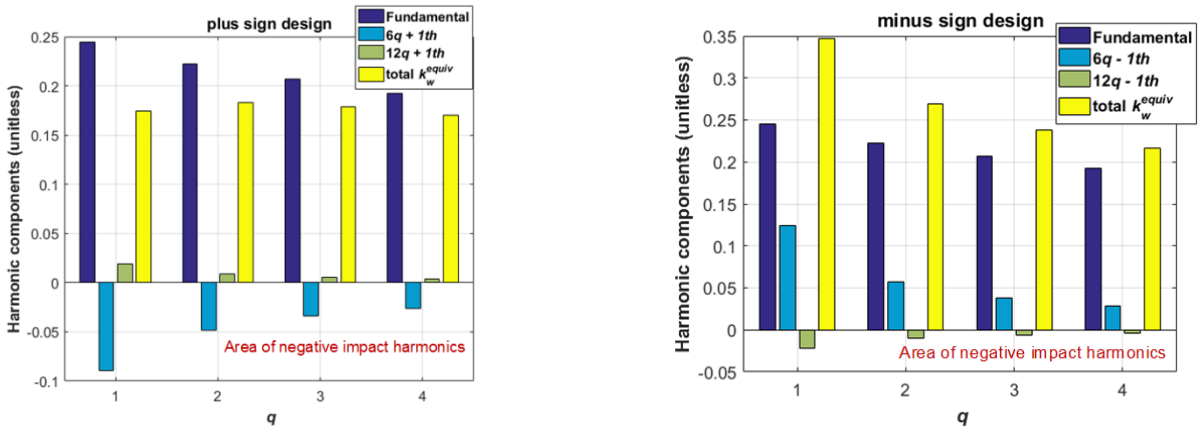

(a) Plus sign design (b) Minus sign design

Fig. 8. Harmonic components of k_w^{equiv}.

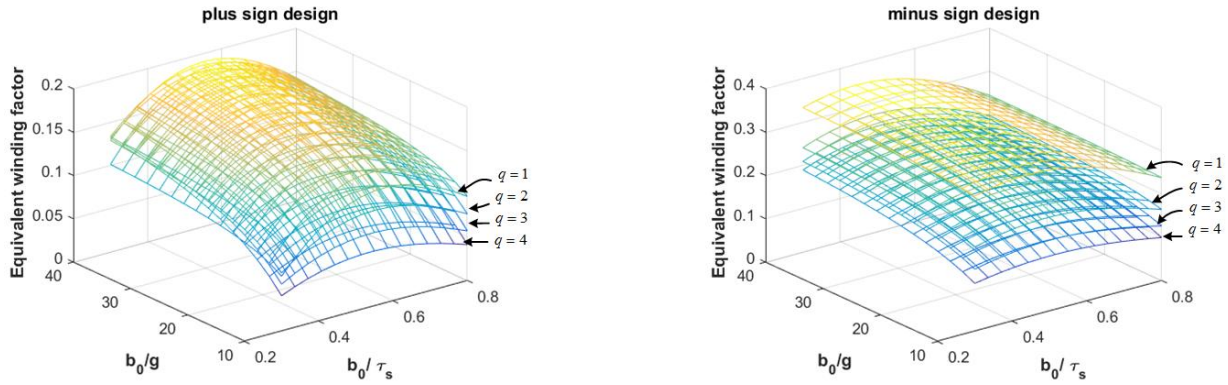

(a) Plus sign design (b) Minus sign design

Fig. 9. Parametric study of k_w^{equiv} including effects from multi-harmonic coupling and stator teeth geometry

It is shown that the winding factor harmonic vector **k** is mainly determined by its SPP value, and the relative permeance vector **p** is determined by the stator slot geometry i.e. $(b_0/\tau_s, b_0/g)$. Thus, a certain choice of these parameters should be made to achieve an optimum equivalent winding factor design which will help increase the back-EMF induction and torque capability.

The multi-harmonic fields coupling effects are evaluated in Fig. 8(a) with the plus sign gear ratio design, and Fig. 8(b) with the minus sign gear ratio design, respectively. The two plots contain both the individual harmonic components (the product of winding factor and relative permeance divided by corresponding harmonic order) and the total value. Here $b_0/\tau_s = 0.5$, $b_0/g = 20$ are assumed such that $\hat{p}_0(b_0/\tau_s, b_0/g)$, and $\hat{p}_1(b_0/\tau_s, b_0/g)$ are kept unchanged to exclude the effects of stator teeth geometry. The magnitude of individual and total harmonic components are compared across different q values ranging from 1 to 4. The results suggest that

This article has been accepted for publication in a future issue of this journal, but has not been fully edited. Content may change prior to final publication. Citation information: DOI 10.1109/TIA.2018.2856579, IEEE Transactions on Industry Applications

the minus sign design generally produces a larger k_w^{equiv} as it has less significant negative harmonics which essentially produce braking torque. It is also preferred to choose q as small as possible, so that the sum of the harmonic components can be maximized by coupling the lowest order harmonics. It should be noted that among the three coupling harmonics, the fundamental harmonic contributes most to the term k_w^{equiv}. Meanwhile, to maximize the back-EMF and torque production, the choice of q value should be evaluated along with B_{m1} and P_r/P_s on a case by case basis, to account for the leakage flux that might be severe for a high pole count design. Geometry constraints may also play an important role as shall be seen in the following design case study.

The analysis can be expanded to include the effects of stator teeth geometry, by implementing a two-dimensional parametric study using ratios b_0/τ_s, and b_0/g, as shown in Fig. 9(a) with plus sign gear ratio design and Fig. 9(b) with a minus sign gear ratio design. A surface mesh plot of k_w^{equiv} can be obtained for different SPP values, where the range of parameters are chosen to cover most machine cases as b_0/g spans the region from 10 to 40, and b_0/τ_s ranges from 0.2 to 0.8. The parametric study provides a consistent result that the minus sign design with a small q value generally produces a larger k_w^{equiv}, which is the characteristic shared by the conventional winding factor. In addition, particular ranges of b_0/τ_s, and b_0/g must be selected for an optimum design.

Thus, based on this study, a maximum k_w^{equiv} design leads to a minus sign gear ratio design with SPP value q = 1, which results in the gear ratio being

$$P_r/P_s = 6q - 1 = 5 \quad (27)$$

IV. Alternating Rotor Leakage Flux Blocking Structure in a Consequent Pole Design

A. Alternating Flux Barrier Structure

As the spoke type structure is considered to be ideal for the adoption of cost-effective ferrite magnets, following the derivations of the previous section, a unity q SPP, 4 stator pole, 20 rotor pole ($P_r/P_s = 5$) ferrite SVPM of the conventional topology and a new proposed topology are shown in Fig. 10. Both of them are consequent pole design, whose dimensions can be found in Table IV. For the conventional topology, as the zoomed-in rotor portion in Fig. 10(a) suggests, the rotor radial space is occupied by ferrite magnets with thin iron bridges on the top and bottom to hold the magnets in place. For the proposed design in Fig. 10(d), where the key design parameters are delineated, an alternating flux barrier structure is now placed on the bottom of pair-wise spoke type magnets. The barriers need to be of low permeability material (or air), which are connected by a thin iron bridge. The iron bridge is preferred which can help limit the axial leakage flux at the rotor ends and eliminate any unbalanced force [22].

The corresponding no load flux line distributions are shown in Fig. 10(b), and (e), where the flux from rotor magnets that links to the coil set A can be extracted by simple inspection. Two major rotor magnet flux paths specified in red and orange that links coil A in the conventional SVPM design can be observed in Fig. 10(b), with colored arrows indicating the corresponding flux direction. By adopting the proposed design, there is three major rotor magnet flux paths, linking four magnets to coil A.

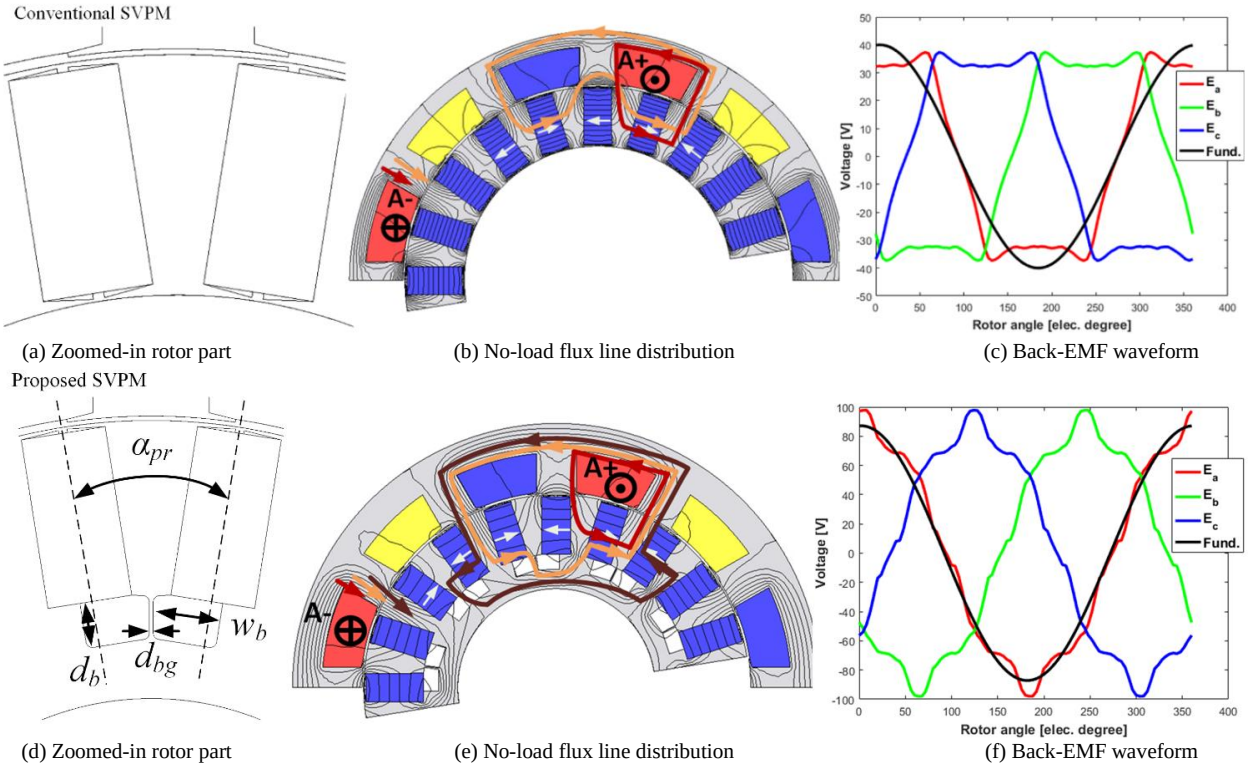

(a) Zoomed-in rotor part (b) No-load flux line distribution (c) Back-EMF waveform

(d) Zoomed-in rotor part (e) No-load flux line distribution (f) Back-EMF waveform

Fig. 10. No-load study comparison of a conventional design and an alternating flux barrier design

This article has been accepted for publication in a future issue of this journal, but has not been fully edited. Content may change prior to final publication. Citation information: DOI 10.1109/TIA.2018.2856579, IEEE Transactions on Industry Applications

The extra iron space created in between pair-wise adjacent magnets is also a part of the flux path colored in brown and helps include two additional magnets to link coil A. It also should be noted that the alternating use of rotor flux barriers allows the use of an enlarged rotor back iron, which in turn, effectively reduces the leakage flux at the rotor inner radius surface. This result is verified by the back-EMF plots in Fig.10(c), and (f), where the fundamental of phase voltage becomes doubled with the same amount of magnet usage and with minimum modification on the rotor. Furthermore, the no-load voltage waveform also becomes more sinusoidal.

B. Performance Comparison of Two Gear Ratio Designs

As indicated by the sizing equations, two gear ratio designs are available for a given SPP value as the plus sign design and the minus sign design. It has been shown that the minus sign design is preferred as it has the larger equivalent winding factor, which will lead to larger back-EMF induction and torque production. A finite element analysis (FEA) based comparison is made between these two ratio designs to validate the developed analytical model. Furthermore, for the proposed alternating flux barrier topology, the rotor pole pitch angle α_{pr} is directly related to the flux path in between rotor magnets, and can be expressed as

$$\alpha_{pr} = \frac{360}{(6q \pm 1) P_s} \tag{28}$$

Hence, to allow for a sufficiently large flux path to enable the alternating flux barrier design, the SPP value q and stator pole number P_s should be kept small.

TABLE III. KEY DIMENSIONS

Key Parameters	Minus sign design	Plus sign design
Output power [kW]	20	20
Magnet material/ B_r [T]	Ferrite/0.45	Ferrite/0.45
Current density J_s [A/mm^2]	4.6	4.6
Stator pole number P_s	4	4
Rotor pole number P_r	20	28
Slot per pole per phase (SPP) q	1	1
Gear ratio P_r/P_s	5	7
Turns per phase N_s	10	10
Slot fill factor K_{cu}	0.4	0.4
Magnet dimension $d \times w$ [mm]	20.8×39.5	12×38.9
Stator *OR/IR* [mm]	177.8/139	177.8/139
Rotor *OR/IR* [mm]	138/95.5	138/95.5
Active stack length [mm]	311.15	311.15
Airgap length [mm]	1	1
Rotor pole pitch angle α_{pr} [°]	12.85	18

Two models with plus and minus gear ratio designs have been developed and the corresponding key dimensions are tabulated in Table. III where the two models share the same stator with a unity SPP value and 4 poles. The rotor pole numbers are different based on the choice of gear ratio, which are $P_r = 7P_s$ for the plus sign design and $P_r = 5P_s$ for the minus sign design. A no load study of two models are shown in Fig. 11. The flux density distribution and flux lines indicate that the minus sign design has a larger flux linkage with the stator coils. On the other hand, instead of linking the stator coils, a considerable amount of leakage flux exists at the airgap surface of the plus sign design.

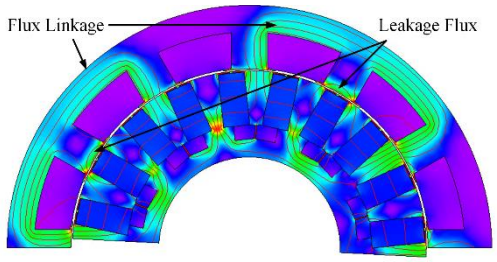

(a) minus sign design

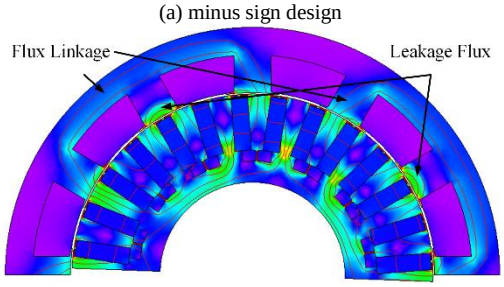

(b) plus sign design

Fig. 11. No-load flux density distribution

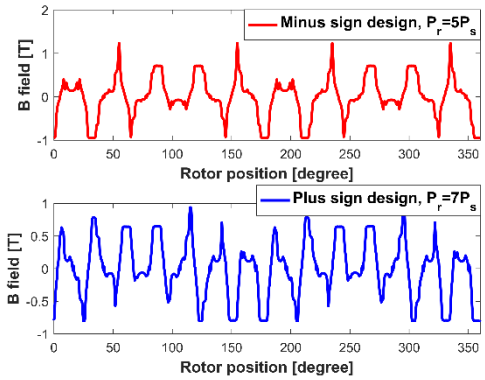

Fig. 12. No-load flux density distribution at the airgap centerline

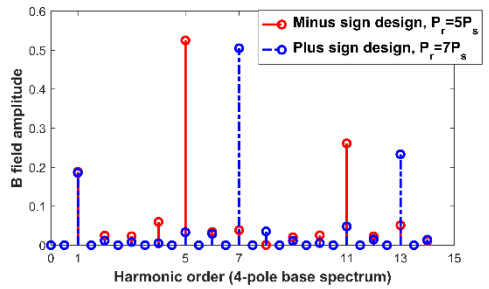

Fig. 13. FFT analysis of no-load flux density distribution at the airgap centerline

To verify the flux modulation effects of the stator teeth, the flux density distribution at the airgap center line around machine circumference is provided in Fig. 12. The results suggest that the flux density of the plus sign design has more variations but with a smaller peak to peak value compared to the minus sign design. A corresponding FFT analysis of spatial flux density distribution is illustrated in Fig. 13, where the harmonic order is based on the stator pole number. It verifies that it is the gear ratio value which determines the flux density distribution in the airgap. For the plus sign design, the three

This article has been accepted for publication in a future issue of this journal, but has not been fully edited. Content may change prior to final publication. Citation information: DOI 10.1109/TIA.2018.2856579, IEEE Transactions on Industry Applications

major flux density harmonics are fundamental, 7th and 13th. For the minus sign design, the three major flux density harmonics are fundamental, 5th and 11th. Both results match very well with the conclusions in Table II.

Comparisons of back-EMF induction and torque production between the plus sign design and minus sign design were carried out using both derived analytical equations and FEA calculations, where the parameters are given in Table III. A 0.4 T is assumed for B_{m1} consistent with the adoption of ferrite magnets. The comparison of the fundamental component of back-EMF in Fig. 14 confirms that the minus sign design has more induced voltage compared to the plus sign design. The analytical equation (21) achieves high accuracy in modelling the two designs, with about 5% difference compared to FEA results for the plus sign design, and less than 6% difference for the minus sign design. The waveforms also verify that the machine synchronous frequency/speed is proportional to the rotor pole number.

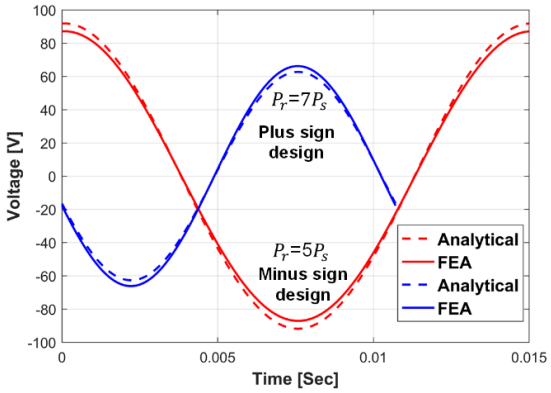

Fig. 14. Back-EMF verification using sizing equation and FEA calculations

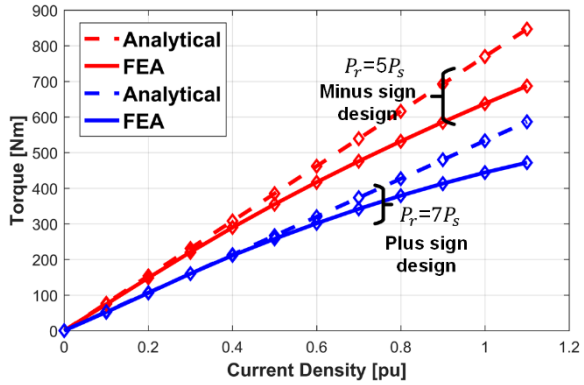

Fig. 15. Torque verification using sizing equation and FEA calculations

Fig. 15 shows a torque vs. current comparison at MTPA (maximum torque per ampere) points, where 1 *pu* current corresponds to 4.6 A/mm^2 current density. The FEA results verify the prediction that the minus sign design will produce more torque compared to the plus sign design. Meanwhile, discrepancies become exaggerated between the analytical model (26) and FEA calculations as current level increases for both designs. The difference is mainly caused by the saturation effects in iron cores, which was ignored in the analytical model.

The FEA calculation results verify the validity of the analytical model for back-EMF and torque production for proposed vernier machine topologies and confirm that the minus sign gear ratio design should be adopted for better performance due to the effect of an equivalent winding factor.

C. Non-salient Electromagnetic Behavior

In general, the proposed alternating flux barrier structure appears to produce reluctance variations on the rotor, which might cause saliency differences such as with an interior magnet PM machine. A study of the stator flux linkage at different rotor positions is presented in Fig. 16 with all the rotor magnets removed, where the flux linkage is extracted from 3-phase windings and converted to the rotor synchronous frame. The results, however, show that the fluctuations of flux linkage along rotor circumference are very limited, i.e. within 10%. This non-salient electromagnetic behavior is further confirmed with a torque vs. current angle study shown in Fig. 17, where the average torque in red circles are marked at different current angles. The waveform profile is very close to the blue dashed pure sine waveform, whose magnitude is the same as the maximum available torque obtained at $\gamma = 0°$ in the FEA model. Thus, the proposed machine such as the one in Fig. 10 needs to be modeled only as a surface PM with no saliency and the torque manipulation can be realized by a simple q-axis current control.

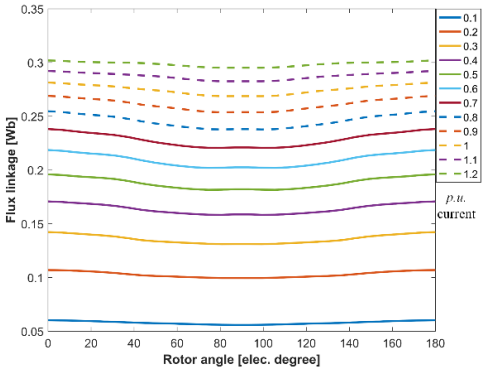

Fig. 16. Stator excited flux linkage at different rotor positions

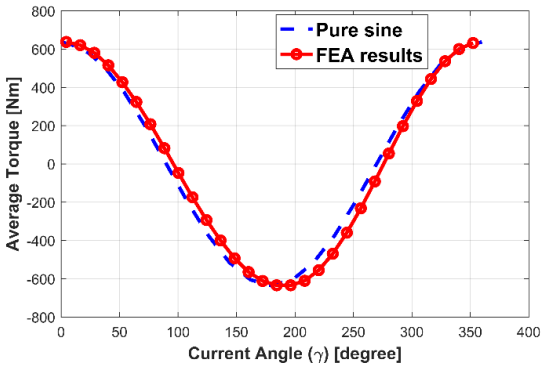

Fig. 17. Torque V.S. current angle of the proposed topology

This article has been accepted for publication in a future issue of this journal, but has not been fully edited. Content may change prior to final publication. Citation information: DOI 10.1109/TIA.2018.2856579, IEEE Transactions on Industry Applications

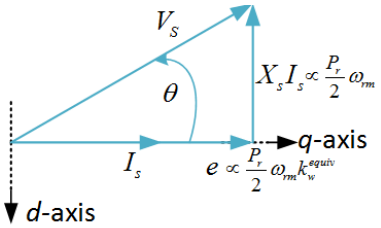

Fig. 18. Phasor diagram of the proposed topology

A corresponding field-oriented vector diagram is shown in Fig. 18, where the voltage across the reactance is proportional to the synchronous speed. The induced voltage is proportional to the product of the synchronous speed and the equivalent winding factor, which would have a negative impact on the power factor as it would decrease along an increasing SPP value. From structural perspective, the non-salient feature of the proposed topology is attributed to the use of different stator and rotor pole number, plus the consequent rotor pole design.

D. Design Case Study

A proposed and conventional SVPM using ferrite magnets have been designed, following the observations obtained in the previous section, for an industrial cooling fan application. To make a fair comparison, the designs are compared with a commercially available benchmark rare earth IPM of a major motor manufacturer. The machine outer stator diameter and stack length are kept the same, as well as the stator current density. A multi-objective FEA optimization is carried out for the proposed and conventional SVPM, to maximize the average torque and minimize the ripple torque, where parametric dimensions of two topologies are identified in Fig. 19. The optimized dimensions are summarized in Table IV with the corresponding 2D model presented in Fig. 20. The results show that the proposed SVPM adopts a smaller split ratio, i.e. ratio between stator inner and outer radius. However, a larger rotor back iron is required to enable the alternating rotor leakage flux blocking feature.

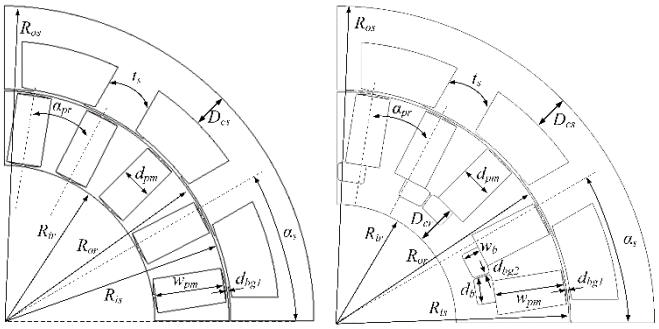

(a) Conventional design (b) Proposed design

Fig. 19. Key design parameters and geometric definitions

A comparison of transient and average torque is provided in Fig. 21(a), between the proposed and conventional design at the rated current excitation, where the average torque is improved by more than 50%, whereas the ripple torque also reduced by about 60%. A torque vs. current evaluation is carried out in Fig. 21(b). The results suggest that the proposed machine using ferrite magnets consistently outperforms the conventional machine in torque production, or equivalently the torque density given the same machine volume. The torque of the proposed machine is even higher than the commercially available benchmark IPM using rare earth magnets at the rated current condition.

TABLE IV. OPTIMIZED KEY DIMENSIONS

	Proposed Design	**Existing Design**
Stator *OR/IR* [mm]	177.8/139	177.8/130.9
Rotor *OR/IR* [mm]	138/95.5	129.8/66.5
Stator back iron length D_{cs} [mm]	19.8	11.3
Rotor back iron length D_{cr} [mm]	13.5	-
Stator teeth pitch angle α_s [°]	30	30
Rotor pole pitch angle α_{pr} [°]	18	18
Stator teeth width t_s [mm]	26.5	26.6
Magnet thickness d_{pm} [mm]	20.8	20
Magnet width w_{pm} [mm]	38.9	39.5
Top leakage bridge length d_{bq1} [mm]	0.5	0.8
Bottom leakage bridge length d_{bq2} [mm]	0.8	0.8
Flux barrier thickness d_b [mm]	14.6	-
Flux barrier width w_b [mm]	10.4	-

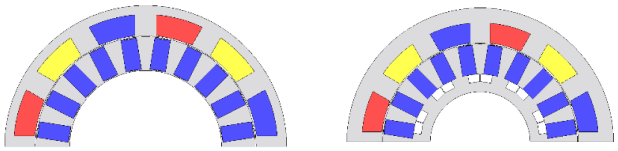

(a) Conventional design (b) Proposed design

Fig. 20. Optimized models

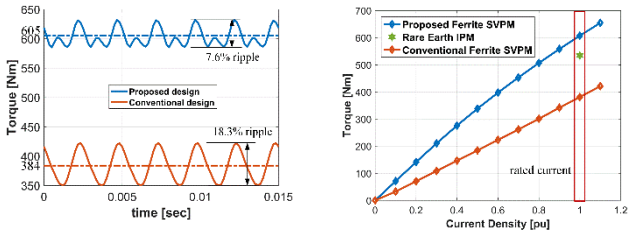

(a) Instantaneous torque (b) Torque vs. current

Fig. 21. Torque performance comparison

TABLE V. PERFORMANCE COMPARISON

	Benchmark Motor	**Proposed Design**	**Conv. Design**
Machine type	IPM	VPM	VPM
Magnet type/B_r [T]	NdFeB/1.2	Ferrite/0.42	Ferrite/0.42
Stator/rotor pole number	4/4	4/20	4/20
SPP	4	1	1
J_s [A/mm^2]	4.6	4.6	4.6
Excitation frequency, [Hz]	13.33	66.67	66.67
PM mass/% of total weight [kg]	11.3/3.6%	25.2/8%	24.8/7.9%
Cu vol. (incl. end wind.) [L]	3.1	3.5	3.74
Torque [Nm]	534	605	384
Torque density [Nm/L]	17.3	19.4	12.2
Power factor [lagging]	0.8	0.62	0.61

To achieve this high torque density level, a detailed performance comparison in Table. V shows that the proposed SVPM requires about twice the weight of ferrite magnets with a somewhat lower power factor, due to the low remanence of the ferrite. The excitation frequency is also increased because of a larger rotor pole number. Meanwhile, only minimum

modifications have been made to the rotor to achieve the degree of performance improvement obtained.

V. Conclusion

A comprehensive analytical model for a generic consequent pole spoke type vernier PM machine has been presented. Physics-based sizing equations were developed where an equivalent winding factor k_w^{equiv} is defined to model flux modulation effects and multi-harmonic fields coupling effects. Two generic gear ratio designs are identified and compared, for a given q value; the minus sign design generally producing a larger k_w^{equiv}. The analytical modeling of back-EMF and torque production were further verified by FEA calculations, from which the non-salient electromagnetic behavior is also identified and studied. Furthermore, a consequent pole alternating flux barrier SVPM using ferrite PMs has been proposed. The FEA results suggest that the proposed SVPM significantly improves the back-EMF/torque production of a conventional SVPM. The torque production even surpasses that of a benchmark rare earth magnet assisted IPM under the same stator current density condition, with the tradeoff being that the magnet weight is increased while the power factor is lowered due to the use of ferrite magnets. Overall, the simple structure and good torque capability make this proposed SVPM an attractive and practical candidate for low-speed applications, such as industrial cooling fans, wind turbines, and marine propulsion.

Acknowledgment

The authors express their gratitude to the companies of the Wisconsin Electric Machines and Power Electronics Consortium (WEMPEC) for assistance and support during this research.

References

[1] G. Kronacher, "Design, performance and application of the Vernier resolver," *The Bell System Technical Journal*, vol. 36, no. 6, pp. 1487–1500, 1957.

[2] C. H. Lee, "Vernier motor and its design," *IEEE Trans. Power Appar. Syst.*, vol. 82, no. 66, pp. 343–349, 1963.

[3] A. Ishizaki, T. Tanaka, K. Takahashi, and S. Nishikata, "Theory and Optimum Design of PM Vernier Motor." Electrical Machines and Drives Seventh International Conf., Durham, UK, 1995.

[4] L. Wu, R. Qu, D. Li, and Y. Gao, "Influence of Pole Ratio and Winding Pole Numbers on Performance and Optimal Design Parameters of Surface Permanent-Magnet Vernier Machines," *IEEE Trans. Ind. Appl.*, vol. 51, no. 5, pp. 3707–3715, Sep. 2015.

[5] Y. Oner, Z. Q. Zhu, L. J. Wu, X. Ge, H. Zhan, and J. T. Chen, "Analytical On-Load Subdomain Field Model of Permanent-Magnet Vernier Machines," *IEEE Trans. Ind. Electron.*, vol. 63, no. 7, pp. 4105–4117, Jul. 2016.

[6] A. Toba and T. A. Lipo, "Novel dual-excitation permanent magnet vernier machine," in *Industry Applications Conference, 1999. Thirty-Fourth IAS Annual Meeting. Conference Record of the 1999 IEEE*, 1999, vol. 4, pp. 2539–2544.

[7] S. Niu, S. L. Ho, W. N. Fu, and L. L. Wang, "Quantitative Comparison of Novel Vernier Permanent Magnet Machines," *IEEE Trans. Magn.*, vol. 46, no. 6, pp. 2032–2035, Jun. 2010.

[8] D. Li, R. Qu, and T. A. Lipo, "High-Power-Factor Vernier Permanent-Magnet Machines," *IEEE Trans. Ind. Appl.*, vol. 50, no. 6, pp. 3664–3674, Nov. 2014.

[9] Z. S. Du and T. A. Lipo, "High torque density ferrite permanent magnet vernier motor analysis and design with demagnetization consideration," in *Energy Conversion Congress and Exposition (ECCE), 2015 IEEE*, 2015, pp. 6082–6089.

[10] W. Liu and T. A. Lipo, "A family of vernier permanent magnet machines utilizing an alternating rotor leakage flux blocking design," in *Energy Conversion Congress and Exposition (ECCE), 2017 IEEE*, 2017, pp. 2461–2468.

[11] E. Spooner and L. Haydock, "Vernier hybrid machines," *IEE Proc. - Electr. Power Appl.*, vol. 150, no. 6, p. 655, 2003.

[12] F. Zhao, T. A. Lipo, and B.-I. Kwon, "A Novel Dual-Stator Axial-Flux Spoke-Type Permanent Magnet Vernier Machine for Direct-Drive Applications," *IEEE Trans. Magn.*, vol. 50, no. 11, pp. 1–4, Nov. 2014.

[13] A. Toba and T. A. Lipo, "Generic torque-maximizing design methodology of surface permanent-magnet vernier machine," *IEEE Trans. Ind. Appl.*, vol. 36, no. 6, pp. 1539–1546, 2000.

[14] B. Kim and T. A. Lipo, "Operation and Design Principles of a PM Vernier Motor," *IEEE Trans. Ind. Appl.*, vol. 50, no. 6, pp. 3656–3663, Nov. 2014.

[15] D. Li, R. Qu, J. Li, L. Xiao, L. Wu, and W. Xu, "Analysis of Torque Capability and Quality in Vernier Permanent-Magnet Machines," *IEEE Trans. Ind. Appl.*, vol. 52, no. 1, pp. 125–135, Jan. 2016.

[16] B. Kim and T. A. Lipo, "Analysis of a PM Vernier Motor With Spoke Structure," *IEEE Trans. Ind. Appl.*, vol. 52, no. 1, pp. 217–225, Jan. 2016.

[17] T. Zou, D. Li, R. Qu, and D. Jiang, "Performance Comparison of Surface and Spoke-Type Flux-Modulation Machines With Different Pole Ratios," *IEEE Trans. Magn.*, vol. 53, no. 6, pp. 1–5, Jun. 2017.

[18] F. W. Carter, "The magnetic field of the dynamo-electric machine," *J. Inst. Electr. Eng.*, vol. 64, no. 359, pp. 1115–1138, 1926.

[19] B. Heller and V. Hamata, *Harmonic Field Effects in Induction Machines*. Amsterdam, The Netherlands: Elsevier, 1977.

[20] Z. Q. Zhu, D. Howe, E. Bolte, and B. Ackermann, "Instantaneous magnetic field distribution in brushless permanent magnet DC motors. I. Open-circuit field," *IEEE Trans. Magn.*, vol. 29, no. 1, pp. 124–135, 1993.

[21] T. A. Lipo, *Introduction to AC Machine Design*, John Wiley/IEEE Press, Hoboken NJ, 2017.

[22] X. Ge, Z. Q. Zhu, J. Li, and J. Chen, "A Spoke-Type IPM Machine With Novel Alternate Airspace Barriers and Reduction of Unipolar Leakage Flux by Step-Staggered Rotor," *IEEE Trans. Ind. Appl.*, vol. 52, no. 6, pp. 4789–4797, Nov. 2016.